Supplement of Earth Surf. Dynam., 13, 71–79, 2025
https://doi.org/10.5194/esurf-13-71-2025-supplement

Earth Surface Dynamics
Open Access
EGU

Supplement of

Evidence of slow millennial cliff retreat rates using cosmogenic nuclides in coastal colluvium

Rémi Bossis et al.

Correspondence to: Vincent Regard (vincent.regard@get.omp.eu) and Sébastien Carretier (sebastien.carretier@get.omp.eu)

S1 Sample processing and ^{10}Be measurements

After sieving at 0.5-1 mm, the magnetic part of the sample was removed with a magnetic separator (Frantz). The chemical treatment then begins by a series of acid attacks with a mixture of concentrated hydrochloric (HCl) and hexafluorosilisic (H_2SiF_6) acids to remove all non-quartz minerals. When the quartz was extracted, meteoric ^{10}Be was removed by three partial dissolutions with concentrated hydrofluoric acid (HF). The decontaminated quartz was finally totally dissolved with concentrated hydrofluoric acid (HF) after adding 500 μL of ^{9}Be carrier solution (Scharlau, [^{9}Be] = 1000 μg g^{-1}). The resulting solutions were evaporated until dryness and the samples were recovered with hydrochloric acid. Then, the samples were precipitated with concentrated ammonia before a successive separation through an anion exchange column to remove the iron and a cation exchange column to discard the Boron and to recover the Beryllium. Finally, the eluted Be was precipitated to $Be(OH)_2$ with concentrated ammonia. This work was carried out at GET (Géosciences Environnement Toulouse).

Then, $Be(OH)_2$ was oxidized to BeO. After target preparation by mixing Niobium powder with the BeO oxide, the ^{10}Be/^{9}Be ratios were measured by Accelerator Mass Spectrometry (AMS) at the French National AMS Facility ASTER of CEREGE in Aix-en-Provence (Arnold et al., 2010). The measured ^{10}Be/^{9}Be ratios were calibrated against a house standard STD-11 with an assigned value of (1.191 $\pm$ 0.013) x 10^{-11} (Braucher et al., 2015). The analytical 1σ uncertainties include uncertainties in the AMS counting statistics, the uncertainty in the standard ^{10}Be/^{9}Be ratio (0.1880% and 0.4172%, for Run 1 and Run 2, respectively, cf. table S1), an external AMS error of 0.5% (Arnold et al., 2010), and chemical blank correction. A ^{10}Be half-life of 1.387 $\pm$ 0.01 Myrs was used (Chmeleff et al., 2010; Korschinek et al., 2010).

Among the samples, VERM4 and VERM5 (see section 3.A) have not been added to the study because of their ^{10}Be concentration lower than the detection limit (Tab. S1). These results for VERM4 and VERM5 can be explained either by the mass of the quartz being too low for the ^{10}Be measurement (Tab. S1), or by an erosion rate too high to allow the recording of a cosmogenic ^{10}Be signal (see section 2.A).

S2 Cliff retreat rate detection limits and potential bias

Here we try to estimate the limits of the method in terms of cliff retreat rates. The upper limit is analytical, being the lower detection limit of ^{10}Be. The upper limit is determined by the geomorphological context and the Holocene sea level history.

S2.1 Upper limit of measurable retreat rate

The smallest measurable concentrations are conditioned by the quality of the chemical preparation and the measurement. The detection limit at ASTER AMS is several thousands of atoms depending on the blank quality. For a limit of 5000 atoms, and a sample of 10 g of quartz, a lower concentration limit can be estimated to $\sim$500 atoms g^{-1}. This lower concentration limit corresponds to the upper limit in terms of measurable retreat rate of about 5 mm yr^{-1}.

S2.2 Lower limit of measurable retreat rate

Low recession rates correspond to high ^{10}Be concentrations, which do not pose any particular problem for measurement. On the other hand, the limit is likely to be set by geomorphic history. The sea level returned to a level close to the present ($\pm$5 m) around 6 kyrs BP (e.g., Bintanja and van de Wal, 2008), leading to a renewed retreat of the cliffs (e.g., Stephenson and Kirk, 2000; Trenhaile, 2002; de Lange and Moon, 2005; Regard et al., 2012), and thus of the cliff erosion. It is expected that the erosion rate of the cliff increased largely around 6 kyrs BP. In terms of the cosmogenic isotope record, it is possible that the concentration currently measured represents a somewhat integrated signal over the two periods (before and after 6 kyr BP).

In order to test the bias introduced, we simulate an increase in erosion rates by a factor of 10 to 200, the latter value being an extreme that is barely plausible (Figure S1). Then we invert the calculated concentration into a constant erosion rate and we

compare this rate with the rate prescribed in the model.

For this we consider an escarpment with a constant slope with a homogeneous erosion rate. Thus, we reduce the escarpment to a depth profile. We consider that the shielding and slope effect on the particle path length at depth z compensate each other as the escarpment slopes are 45^o in average (DiBiase, 2018). We then solve Equation 1 to find the ^{10}Be concentration C for 120 points with one point every $dz = 1$ cm at depth. So the simulated depth profile is 12 m in total.

Table S1. ^{10}Be concentration measurements. "<DL" means "Below detection limit".

Sample	Lat (°N)	Long (°E)	Elevation (m)	Quartz mass (g)	^{9}Be added mass (mg)	^{9}Be added (atoms)	^{9}Be added, error (atoms)	Measured ^{10}Be/^{9}Be ratio	Measured ^{10}Be/^{9}Be ratio, error	Measured ^{10}Be (atoms)	Measured ^{10}Be, error (atoms)	^{10}Be corrected of chemical blank	^{10}Be corrected of chemical blank, error	^{10}Be concentration (atoms g^{-1})	^{10}Be concentration, error (atoms g^{-1})
Run 1															
VERM1	42.49926	3.13484	5	2.94	0.5209	3.4842E+19	1.0366E+17	7.8825E-15	5.9674E-16	2.75E+05	2.08E+04	3.38E+04	2.84E+04	11495	9662
VERM2	42.49638	3.13239	5	7.00	0.5195	3.4749E+19	1.0338E+17	8.6910 E-15	6.4313E-16	3.02E+05	2.24E+04	6.12E+04	2.96E+04	8736	4224
VERM3	42.49391	3.13232	10	6.36	0.5198	3.4769E+19	1.0344E+17	1.2771E-14	6.7238E-16	4.44E+05	2.34E+04	2.03E+05	3.04E+04	31946	4775
VERM4	42.47193	3.15398	7	1.71	0.5181	3.4655E+19	1.0311E+17	5.8234E-15	4.5498E-16	2.02E+05	1.58E+04	-3.90E+04	2.50E+04	< DL	
VERM5	42 .39102	3.15390	3	2.27	0.5205	3.4816E+19	1.0358E+17	6.0671 E-15	6.0233E-16	2.11E+05	2.10E+04	-2.96E+04	2.85E+04	< DL	
BRAV1	41.76295	2.99443	4	32.22	0.5205	3.4816E+19	1.0358E+17	1.3262E-14	1.0138E-15	4.62E+05	3.53E+04	2.21E+05	4.03E+04	6855	1250
BRAV3	41.76090	2.98738	3	30.04	0.5213	3.4869E+19	1.0374E+17	1.2336E-14	6.9339E-16	4.30E+05	2.42E+04	1.89E+05	3.10E+04	6301	1031
BRAV4	41 .75500	2.97478	3	15.05	0.5150	3.4448E+19	1.0249E+17	1.0659E-14	6.3190 E-16	3.67E+05	2.18E+04	1.26E+05	2.91E+04	8394	1936
BRAV5	41.70699	2.89881	3	13.26	0.5217	3.4896E+19	1.0382E+17	2.3487 E- 14	1.0059E-15	8.20E+05	3.52E+04	5.79E+05	4.01E+04	43646	3028
BLANK-run1					0.5159	3.4508E+19	1.0267E+17	6.9796 E-15	5.5998E-16	2.41E+05	1.93E+04				
Run 2															
BRAV2	41.76149	2.99260	4	2.98	0.5191	3.4722E+19	1.0331E+17	4.1439E-15	2.6107E-16	1.44E+05	9.07E+03	3.26E+04	1.20E+04	10951	4014
COSTA1	-16.28077	-73.45072	15	2.84	0.5215	3.4883E+19	1.0378E+17	3.6606 E-15	2.4160E-16	1.28E+05	8.44E+03	1.64E+04	1.15E+04	5788	4044
COSTA2	-16.24747	-73.54837	47	4.27	0.5201	3.4789E+19	1.0350E+17	1.4448E-14	6.2128E-16	5.03E+05	2.17E+04	3.91E+05	2.30E+04	91661	5392
COSTA3	-16 .23203	-73 .58788	103	10.38	0.5193	3.4735E+19	1.0334E+17	4.2685 E-14	1.5366E-15	1.48E+06	5.36E+04	1.37E+06	5.41E+04	132121	5214
BLANK-run2					0.5161	3.4521E+19	1.0271E+17	3.2227E-15	2.2559E-16	1.11E+05	7.79E+03				

$$\frac{dC}{dt} = -\lambda C + P \quad (1)$$

$$P = (P_{sp}\, e^{-\rho z/\Lambda_{sp}} + P_{sm}\, e^{-\rho z/\Lambda_{sm}} + P_{fm}\, e^{-\rho z/\Lambda_{fm}}) \quad (2)$$

Where the subscripts of ^{10}Be production rate P refer to the contributions of spallation ('sp'), slow muons ('sm') and fast muons ('fm'). Λ_{sp}, Λ_{sm} and Λ_{fm} [M L^2] are the respective attenuation factors with depth ($\Lambda_{sp} = 150$ g cm^{-2}, $\Lambda_{sm} = 1500$ g cm^{-2}, $\Lambda_{fm} = 4320$ g cm^{-2}) (Braucher et al., 2003). P_{sp}, P_{sm} and P_{fm} are calculated using the same equations as in our manuscript based on Braucher et al. (2003) and Stone (2000). The density $\rho = 2.6$ g cm^{-3}.

We divide time into periods of constant erosion rate. The initial state is a ^{10}Be concentration profile corresponding to an equilibrium profile given by the stationary solution of Equation 1, using the erosion rate of the first period. For each period of time, the time step dt is chosen so that the eroded layer with the specified erosion rate is 1 cm (dz). At each time step, the ^{10}Be concentrations stack is raised from dz and the ^{10}Be concentration is updated at each depth point by removing the radioactive decay and by adding the ^{10}Be production during the time step. The deeper point is assigned a ^{10}Be concentration of 0 at g^{-1}. We can vary the erosion rate from a period to another and track the ^{10}Be concentration at the surface through time.

To calculate the apparent constant erosion rate from this surface ^{10}Be concentration, we use the same Equation (5) as we used to calculate our erosion rate in the manuscript. The relative difference between this erosion rate and the true instantaneous erosion rate is used to calculate the bias shown in Figure S1. In the worst case, the erosion rate is underestimated by 80%, so that it is unlikely that our estimates are biased by more than a factor 2.

We conclude from these tests that in the case where the retreat velocity increased 6 kyrs ago, the measurement made today truly reflects the real value to the correct order of magnitude. However, it should be noted that the lower the recession rates, the longer the integration time, which can be much longer than the Holocene (see Table 1). We recommend a use limited to integration times lower than 10-20 kyrs; it corresponds to retreat rates velocities ϵ exceeding 0.03-0.05 mm yr^{-1}.

S2.3 The case of BRAV2

BRAV2 is the only sample for which sediment could come from above the studied escarpment. Half of the drainage area A is located in the hills above the escarpment. If the hills area erodes very slowly compared to the coastal escarpment, then sediment coming from this area could lower our estimation of the escarpment erosion rate. In order to quantify this bias, we propose the following first-order model. We consider that the hills area and the escarpment area erode at two different rates ϵ_1 and ϵ_2. Their respective mean production rates are $P_1 = 6$ at g^{-1} yr^{-1} and $P_2 = 4.4$ at g^{-1} yr^{-1}. We consider only spallation and we neglect radioactive decay. The mean ^{10}Be concentration of the sampled sediment can be written as the ratio between the flux of ^{10}Be and the flux of quartz:

$$\bar{C} = \frac{A/2}{A/2} \cdot \frac{\epsilon_1 C_1 + \epsilon_2 C_2}{\epsilon_1 + \epsilon_2} \quad (3)$$

and assuming steady state

$$C_1 = \frac{L P_1}{\epsilon_1} \quad (4)$$

$$C_2 = \frac{L P_2}{\epsilon_2} \quad (5)$$

$$(6)$$

where L is the spallation length scale ($\sim$0.65 m). Inserting these equations into the previous one, and solving for ϵ_2:

$$\epsilon_2 = \frac{L(P_1 + P_2)}{\bar{C}} - \epsilon_1 \tag{7}$$

The last equation gives the correct value of ϵ_2, the erosion rate of the coastal escarpment. We can compare it to our estimation which neglects the contribution of the hills area. Our estimation of ϵ_2 is ϵ_{2est} (here neglecting the contribution of muons):

$$\epsilon_{2est} \sim \frac{LP_2}{\bar{C}} \tag{8}$$

Comparing expressions for ϵ_2 and ϵ_{2est} shows that their relative difference is essentially set by the ratio P_1/P_2, in particular if ϵ_1 is very small compared to ϵ_2. It turns out that the relative error of ϵ_{2est} compared to ϵ_2 is necessarily smaller than -60% in absolute terms. We conclude that the potential contribution of the hills above the escarpment cannot change the order of magnitude of our estimated erosion rate for the escarpment above BRAV2 sample.

S2.4 Summary

The method presented here allows to quantify the erosion rate of slowly evolving cliffs (0.05 to 5 mm yr^{-1}). In this, it fills a gap, since it is estimated that the methods currently used are effective for velocities higher than 1 cm yr^{-1}. We can note here that this gap is not completely filled since an alternative method for velocities of about 0.5-1 cm yr^{-1} would be welcome.
The presented method performs an integration of the signal over periods ranging from a century (erosion rate ~ 5 mm yr^{-1}) to about ten thousand years (erosion rate ~ 0.05 mm yr^{-1}). In this last case, the integration covers two episodes of the cliff history characterized by retreat rates likely to be quite different: we have verified that the bias introduced does not exceed an order of magnitude.

S3 Site description

S3.1 VERM and BRAV series

During November 8 and 9, 2021, two sampling series have been carried out on the Mediterranean coast of eastern Pyrenees, between France and Spain (Figure S2), by Rémi Bossis and Vincent Regard. During this campaign, 10 samples have been collected: 5 constituting the "VERM" series (VERM1, VERM2, VERM3, VERM4 and VERM5 on the French coast) and 5 constituting the "BRAV" series (BRAV1, BRAV2, BRAV3, BRAV4 and BRAV5, on the Spanish coast). VERM4 and VERM5 have not been added to the study because of their lower ^{10}Be concentration than the detection limit (see section 1 and Tab. S1).

S3.1.1 VERM series

The samples of the VERM series (for "Côte Vermeille") have been collected, except for VERM5, next to the city of Banuyls-sur-Mer, France (Figure S3), on 8 November 2021. The VERM5 sample has been collected about 10 kilometers to the south, south of the French-Spanish border, the same day. Figure S4 shows geomorphological observations and interpretations on the cliffs for sample sites VERM1, VERM2 and VERM3. The rest of this section transcribes and illustrates the notes taken on the field for each VERM sample.

VERM1:
Location: creek north of Cap d'Ullastrell, 2 km to the north of Banyuls-sur-Mer (Figs. S4 and S5).
GPS coordinates: 42.49926°N / 3.13484°E
Altitude: about 5 m above sea level
Cliff height: 15-20 m
Slope: 41°

Sampling: 6 points spaced about 3 to 5 m apart, consisting of mm- to cm-sized shale grains of light brown to grey colour.
Lithology, after the French geological map of Argelès-sur-Mer (scale 1:50 000): kE1: Alós d'Isil formation, generally greenish and banded pelites and sandstone-pelites.

VERM2:
Location: 350 m southwest of Cap d'Ullastrell (Figs. S4, S6 and S7).
GPS coordinates: 42.49638°N / 3.13239°E
Altitude: about 5 m above sea level
Cliff height: 20-30 m
Slope: 42°
Sampling: 6 points spaced about 5-7 m apart, consisting of mm- to cm-sized sized shale grains, light brown to grey in colour.
Lithology, after the French geological map of Argelès-sur-Mer (scale 1:50 000): Alós d'Isil formation, generally greenish and banded pelites and sandstone-pelites.
Remarks: Possible landslide of a few metres of the cliff sampled along a hundred metres of shoreline (Figure S6 and S7).

VERM3:
Location: 350 to 400 m south of the VERM2 site, about 200 m north of Cap Castell de Velló (Figure S4 and S8).
GPS coordinates: 42.49391°N / 3.13232°E
Altitude: about 10 m above sea level
Height of the cliff: 30-40 m
Slope: 46°
Sampling: 5 points scattered over about 50 metres, consisting of mm- to cm-sized shale grains, light brown to grey in colour.
Lithology, after the French geological map of Argelès-sur-Mer (scale 1:50 000): Alós d'Isil formation, generally greenish and banded pelites and sandstone-pelites.
Remarks: smaller colluvium than at the VERM1 and VERM2 sites and consolidated by grass. We conclude that the cliff is probably less active than at the VERM1 and VERM2 sites. Large boulders and a platform raised by a few metres are protecting the base of the cliff (Figure S8).

VERM4:
Location: between Cap de la Vella and Cap RederÍs, 2 km east-southeast of Banyuls-sur-Mer (Figs. S3, S9 and S10).
GPS coordinates: 42.47193°N / 3.15398°E
Altitude: 7-8 m above sea level
Cliff height: 15-20 m
Slope: 60°
Sampling: 2 points spaced 3 m apart, consisting of mm- to cm-sized shale grains, light brown to grey. Sparse colluvium.
Lithology, after the French geological map of Argelès-sur-Mer (scale 1:50 000): kE1: Alós d'Isil formation, generally greenish and banded pelites and sandstone-pelites.
Remarks: steep cliff with a rocky platform dominating the sea by about 5 m, with large blocks and very little fine sediment. Colluvium collected high on the raised platform, somewhat sheltered from the waves (Figure S9). Possibly also a cliff detachment, as for VERM2 (Figure S10).

VERM5:
Location: small creek south of Garvet beach, about 1.5 km south of Colera, Spain (Figure S11 and S12).
GPS coordinates: 42.39102°N / 3.15390°E
Altitude: 3-4 m above sea level
Cliff height: 10-15 m
Slope: not measured (probably around 40°)
Sampling: 4 points spaced 3 to 5 m apart, consisting of mm- to cm-sized shale grains, light brown to grey colour.
Lithology: Catalan geological map "Llançà" at 1:50 000: ÇOrp3: "Pelites negres amb intercalacions gresoses o limolitiques".

Remarks: site not initially selected because of questionable morphology and a non-negligible risk of contamination from the materials from above the cliff. Indeed, a road is built about 15 m from the top of the cliff (Figure S11 and S12), the construction of which may have released some fresh material.

S3.1.2 BRAV series

The samples of the BRAV series (for "Costa Brava") have been collected, except for BRAV5, next to the small city of Canyet de Mar, Spain (Figure S13), on 9 November 2021. The BRAV5 sample has been collected next to Cap de Bou, about 10 kilometers to the southwest, the same day. Figure S14 shows geomorphological observations and interpretations on the cliffs for sample sites BRAV1, BRAV2 and BRAV3. The rest of this section transcribes and illustrates the notes taken on the field for each BRAV sample.

BRAV1:
Location: Cala Joana, cove located 3.5 km southwest of Sant Feliu de Guíxols and 1 km east of Canyet de Mar (Figs. S13, S14 and S15).
GPS coordinates: 41.76295°N / 2.99443°E
Altitude: 3-5 m above sea level
Cliff height: 100-120 m
Slope: 53°
Sampling: 6 points spaced 5-10 m apart, consisting of mm- to cm-sized gravels, ochre colour. Large colluvium cones flowing onto a pebble beach.
Lithology: Catalan geological map "Baix Empordà" at 1:50 000: Glg: "Leucogranits de gra groller".

BRAV2:
Location: Es Dofinet de Terra, about 200 m southwest of Cala Joana (Figs. S14 and S16).
GPS coordinates: 41.76149°N / 2.99260°E
Altitude: 3-5 m above sea level
Cliff height: 80-100 m
Slope: 45°
Sampling: 4 points spaced 3 to 4 m apart, consisting of mm- to cm-sized gravel, ochre colour.
Lithology: Catalan geological map "Baix Empordà" at 1:50 000: Glg: "Leucogranits de gra groller".
Remarks: cliff protected by large granite blocks, the platform appears locally at the base of the cliff (Figure S16). Cementing of some pebbles gravels by concretions of biological origin. Site not initially selected because of a non-negligible risk of contamination from the materials from above the cliff (Figure S14).

BRAV3:
Location: 50 to 100 m east of Punta dels Canyerets, about 400 m west of BRAV2 (Figure S14 and S17).
GPS coordinates: 41.76090°N / 2.98738°E
Altitude: 3-4 m above sea level
Cliff height: 80-100 m
Slope: 48°
Sampling: 5 points, 4 spaced 4-5 m apart in the east and 1 spaced about 30 m apart, the most westerly. mm- to cm-sized irregular grains, light brown colour.
Lithology: Catalan geological map "Baix Empordà" at 1:50 000: Glg: "Leucogranits de gra groller".
Remarks: unlike the large boulders of the BRAV2 site, the BRAV3 site exhibits smaller boulders and pebbles (Figure S14 and S17). Large black to greenish xenoliths in granites.

BRAV4:
Location: Caleta de Concagrats, small cove 800 m southwest of Canyet de Mar (Figs. S13, S18 and S19).
GPS coordinates: 41.75500°N / 2.97478°E
Altitude: 3-4 m above sea level
Height of the cliff: 60-80 m
Slope: 55°
Sampling : 6 points spaced 5 to 7 m apart, consisting of mm- to cm-sized grains of brown color.
Lithology: Catalan geological map "Baix Empordà" at 1:50 000: Glg: "Leucogranits de gra groller".
Remarks: quartz-rich colluvium over granite blocks on top of a beach made of coarse ochre sand (Figure S18). Numerous pegmatites and xenoliths. A road is built about ten meters from the top of the cliff (Figure S19).

BRAV5:
Location: Southern end of the Platja de Portopí, about 100 m northwest of Cap de Bou (Figs. S20 and S21).
GPS coordinates: 41.70699°N / 2.89881°E
Altitude: 3-4 m above sea level
Cliff height: 40-60 m
Slope: 54°
Sampling: 4 points spaced about 10 m apart.
Lithology: Catalan geological map "Selva" at 1:50 000: Ggd: "Granodiorites and alkaline granites".
Remarks: heavily vegetated cliff, with many trees, making it difficult to observe the cliff top (Figure S20). Presence of dwellings above the cliff, but not directly upstream of the sampling site, about 50 m further north (Figure S21).

S3.2 COSTA series

At the same time as the campaign on the Mediterranean coast of eastern Pyrenees, another sampling campaign was carried out on the Pacific coast of south Peru, southeast of the city of Atico (Figure S22), by Sébastien Carretier. During this campaign, 3 samples have been collected (COSTA1, COSTA2 and COSTA3), forming the "COSTA" series. The rest of this section transcribes and illustrates the notes taken on the field for each COSTA sample.

COSTA1:
Location: Around 20 km south of Atico, from the main road along the coastline (Figs. S22 and S23).
GPS coordinates: -16.28077°N / -73.45072°E
Altitude: 15 m above sea level
Height of the cliff: 340-400 m
Sampling: multiple points along a 50 m stretch of the cliff base.
Remarks: the slope is very steep (Figure S23).

COSTA2:
Location: Around 10 km south of Atico, over a narrow marine terrace (Figure S22).
GPS coordinates: -16.24747°N / -73.54837°E
Altitude: 47 m above sea level

COSTA3:
Location: at the southern entrance of Atico (Figs. S22 and S24).
GPS coordinates: -16.23203°N / -73.58788°E
Altitude: 103 m above sea level
Remarks: very wide marine terrace. Sampling on the inflection point of the slope to avoid the sedimentation zone (Figure S24).

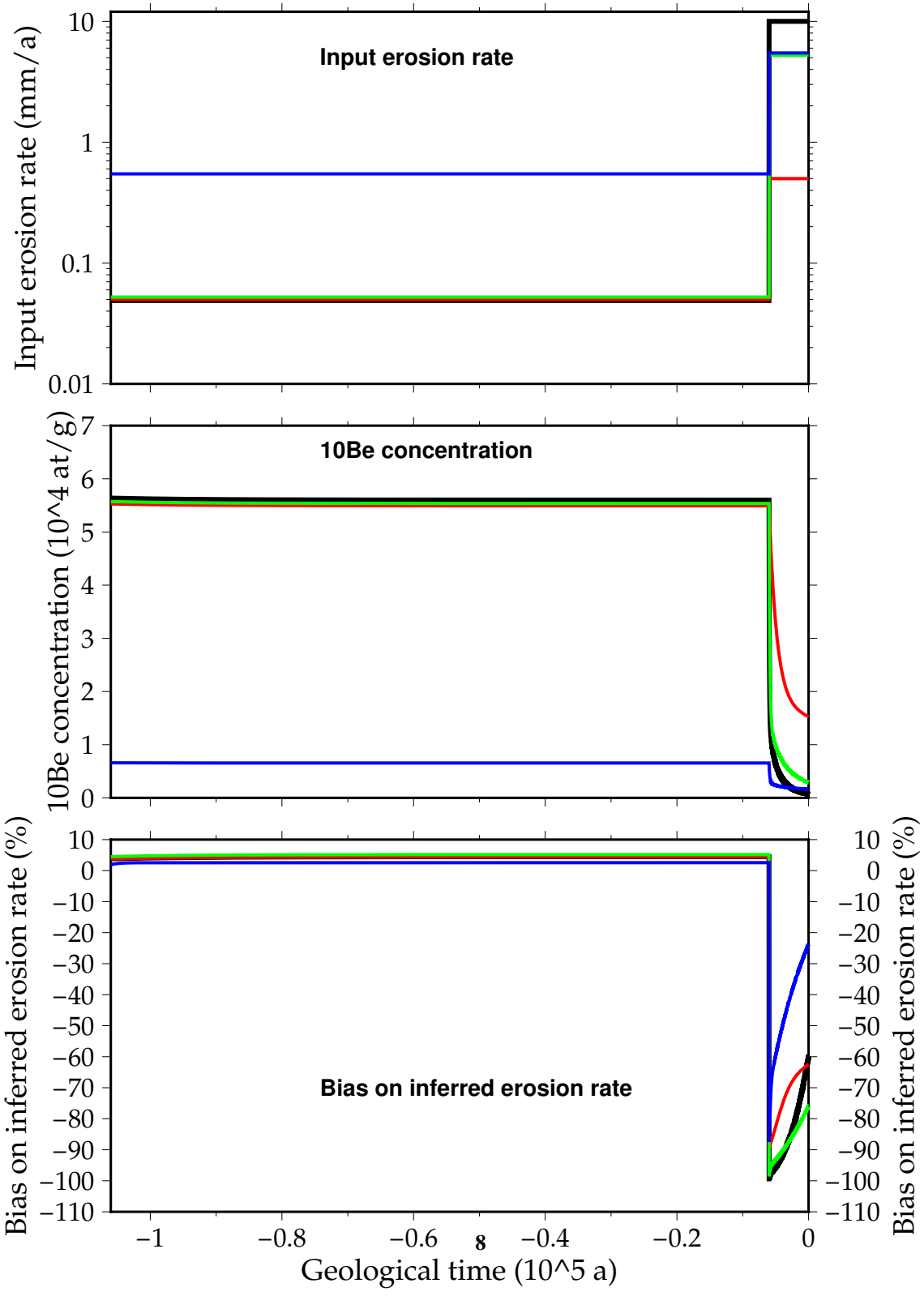
Input erosion rate
Input erosion rate (mm/a)
10
1
0.1
0.01
10Be concentration
10Be concentration (10^4 at/g)
7
6
5
4
3
2
1
0
Bias on inferred erosion rate
Bias on inferred erosion rate (%)
10
0
−10
−20
−30
−40
−50
−60
−70
−80
−90
−100
−110
−1
−0.8
−0.6
−0.4
−0.2
0
Geological time (10^5 a)

Figure S1. (Previous page) Simulations of the ^{10}Be concentration variation (central panel) associated with imposed variations in the erosion rate (top panel), and bias on the inferred erosion rate from these ^{10}Be concentrations assuming a secular equilibrium between ^{10}Be gain and loss (bottom panel), as we assume for real data. In these simulations, during 100 kyrs, the erosion rate is set constant; two values are tested (0.05, in red, green and black and 0.5 mm yr^{-1}, in blue). Then the input erosion is multiplied by 10, 100 or 200 (up to 0.5 mm yr^{-1}, red line, 5 mm yr^{-1}, blue and green lines, and 10 mm yr^{-1}, black line) in the last 6 kyrs, corresponding to the current sea-level highstand (e.g., Bintanja and van de Wal, 2008). To calculate the ^{10}Be concentration, the production rate is fixed at 3.7 at g^{-1} yr^{-1} (sea-level at high latitude), and the ^{10}Be production includes neutrons, fast muons and stop muons as per Braucher et al. (Braucher et al., 2003). The bottom panel shows the evolution of the bias when inferring the erosion rate from the ^{10}Be concentration, as we do with real data. Note that in the case of a low initial erosion rate, the bias is slightly larger than 0 because the equation used to infer the erosion rate does not account for the radioactive decay. The predicted bias in our data can be read on the right y-axis of the bottom panel. In the worst case, the erosion rate is underestimated by 80% (green line). It is thus unlikely that our small erosion rates are underestimated by as much as one order of magnitude.

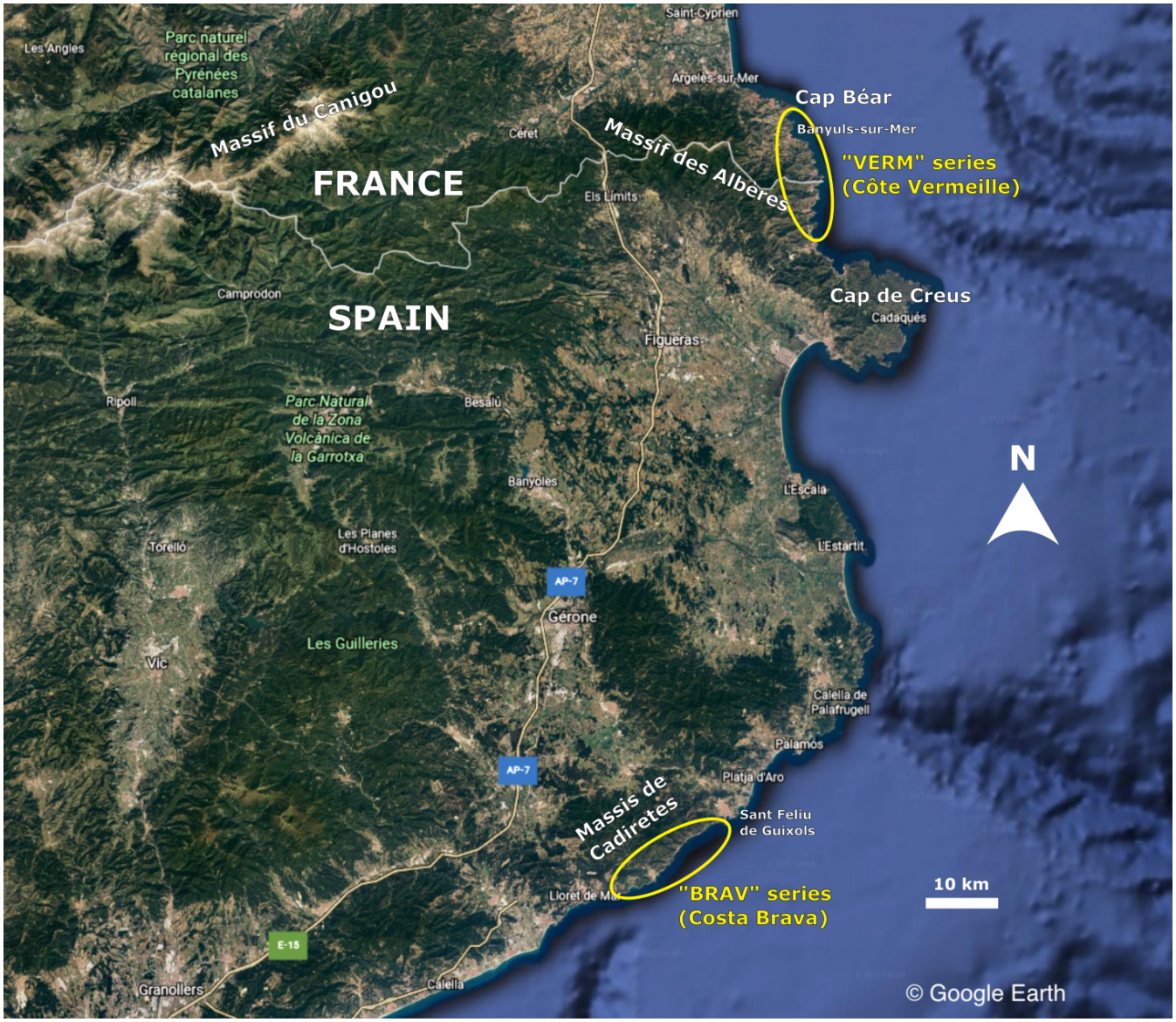

Figure S2. Satellite image (© Google Earth) showing location of the two sampling series carried out on the Mediterranean coast of the easthern Pyrenees, between France and Spain.

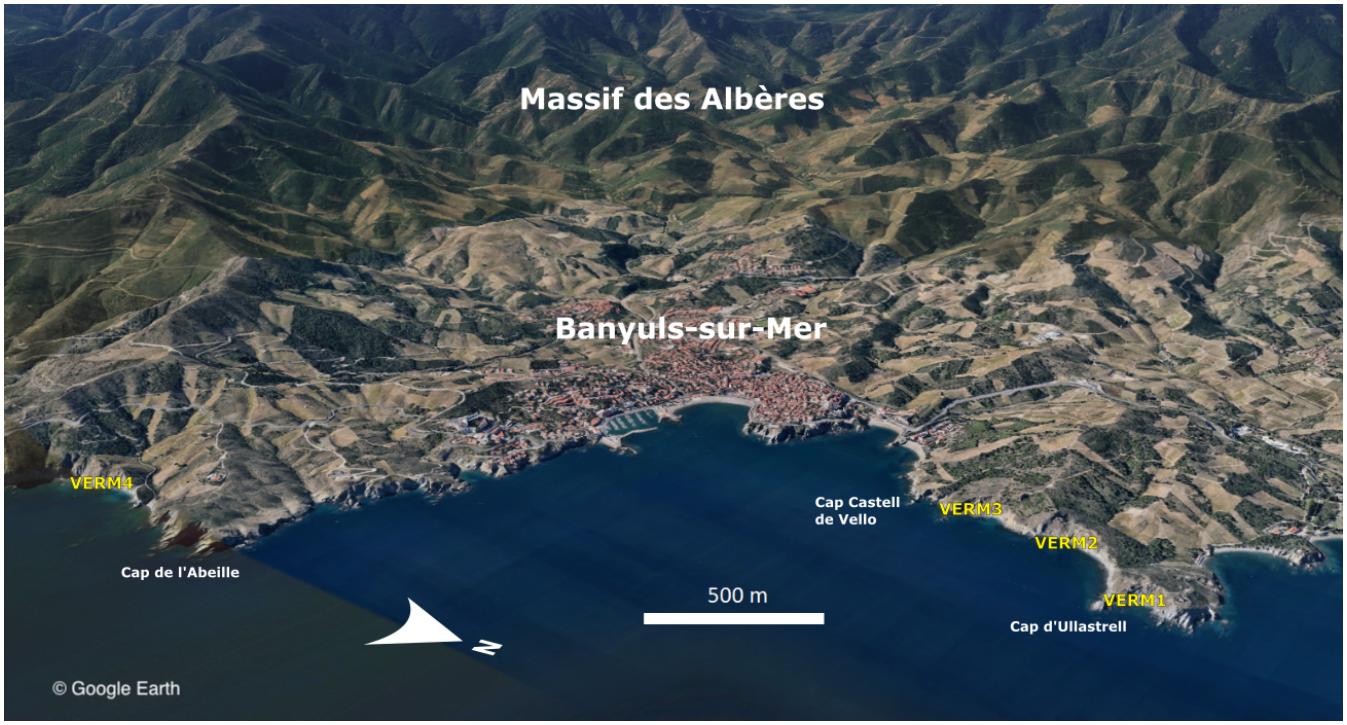

Figure S3. 3D view (© Google Earth) of the coast around Banyuls-sur-Mer. Locations of VERM1, VERM2, VERM3 and VERM4 are indicated in yellow.

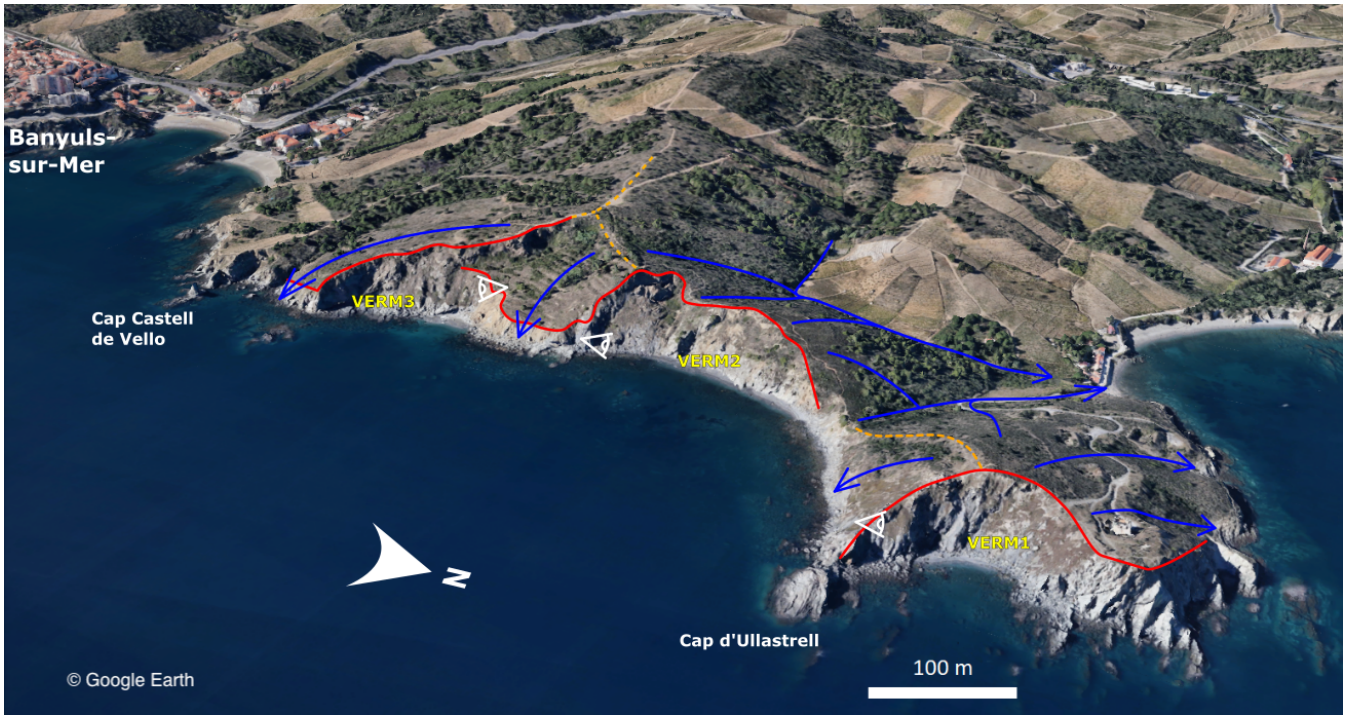

Figure S4. 3D view (© Google Earth) of the cliffs for VERM1, VERM2 and VERM3 (yellow). Red lines are interpreted cliffs top. Orange dashed lines are interpreted crests lines. Blue arrows are flow directions of the runoff water, interpreted from topography. White eye figures show locations and direction of pictures for each sample site.

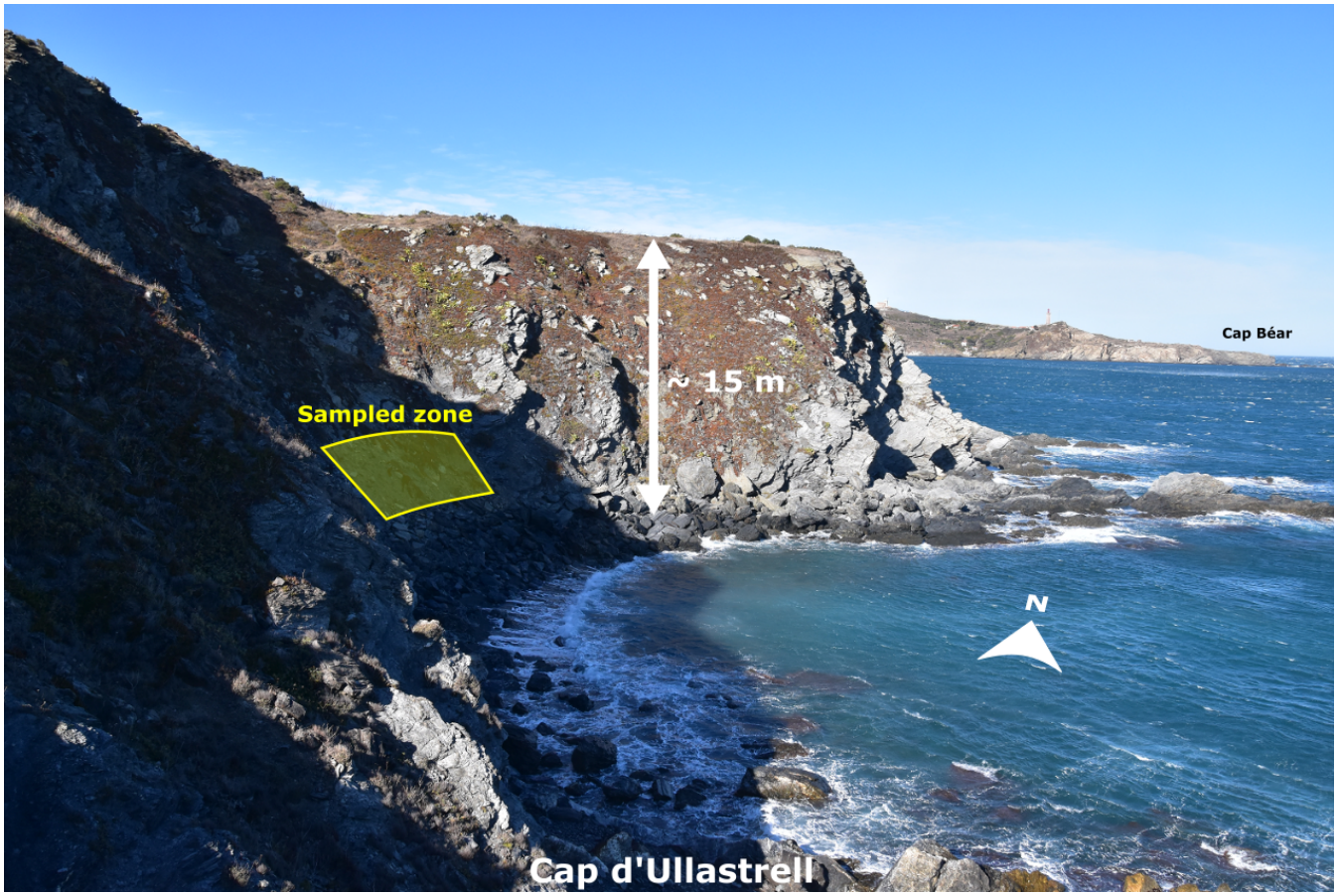

Figure S5. Picture of the VERM1 sample site, seen from the south.

Figure S6. Interpreted picture of the VERM2 sample site, seen from the south.

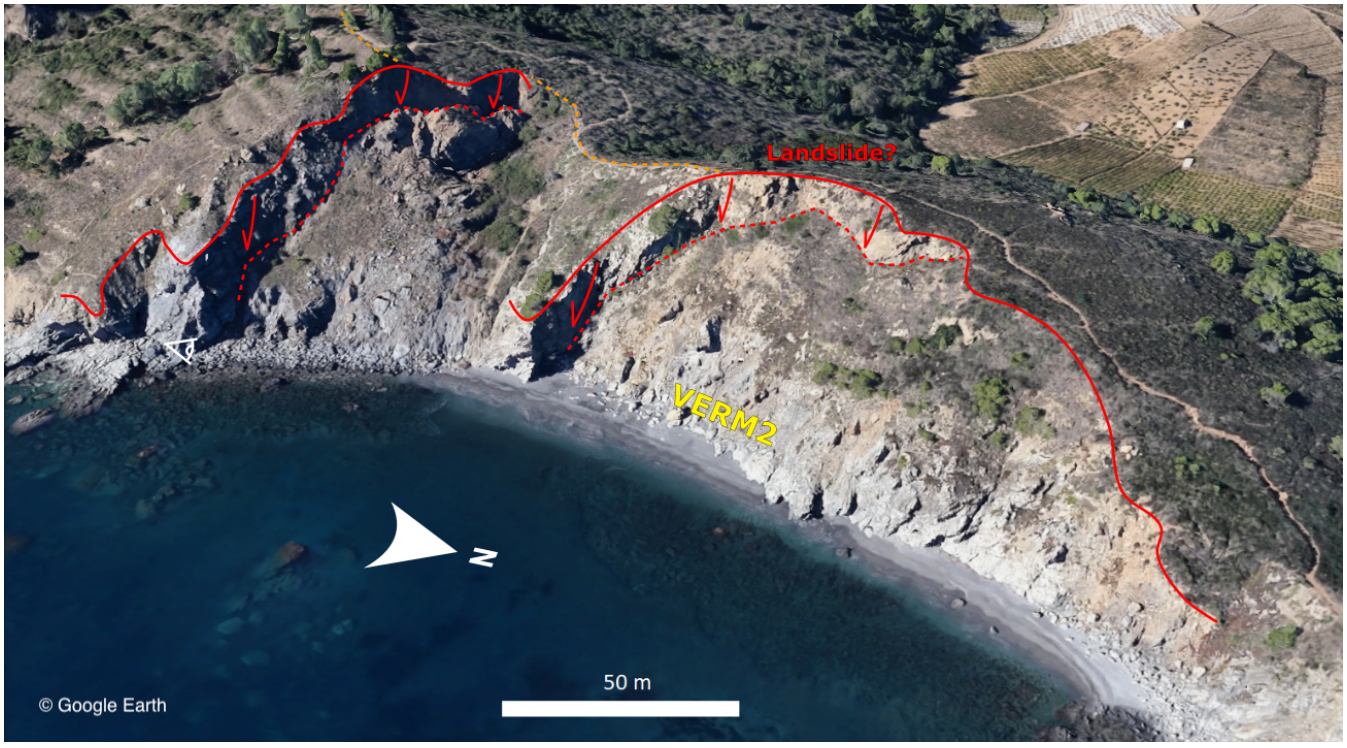

Figure S7. Interpreted 3D view (© Google Earth) of the cliff on the VERM2 sample site (yellow). Red lines are interpreted cliffs top. Orange dashed lines are interpreted crests lines. Red arrows show the possible movement of the cliff. The white eye figure shows the location and the direction of the picture in Figure S6.

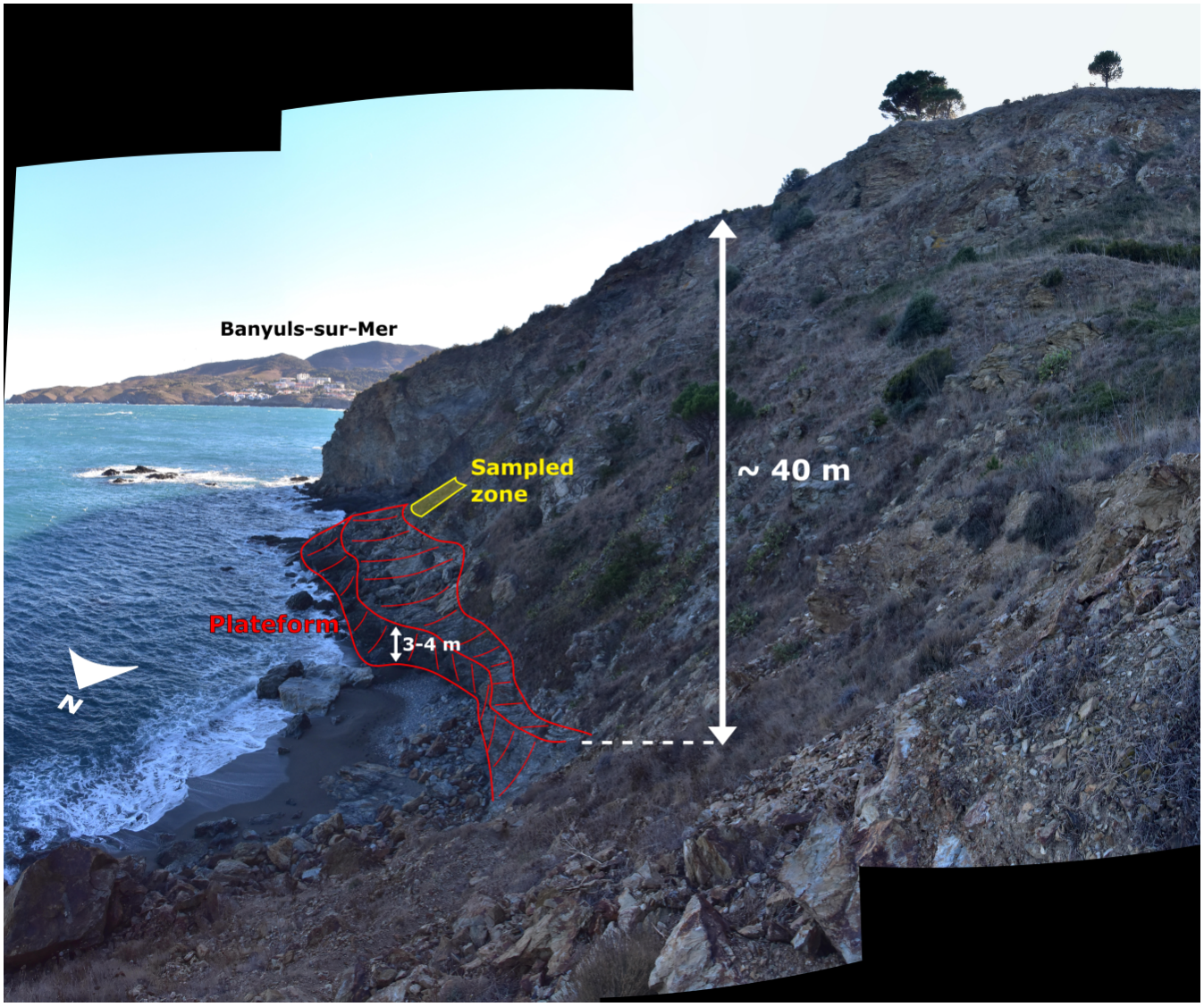

Figure S8. Interpreted mosaic picture for the VERM3 sample site, seen from the north.

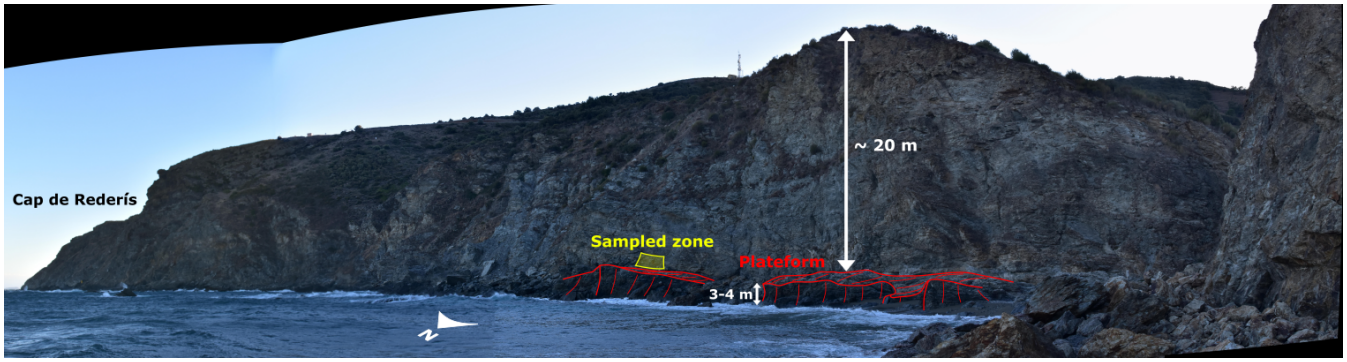

Figure S9. Interpreted mosaic picture for the VERM4 sample site, seen from the north.

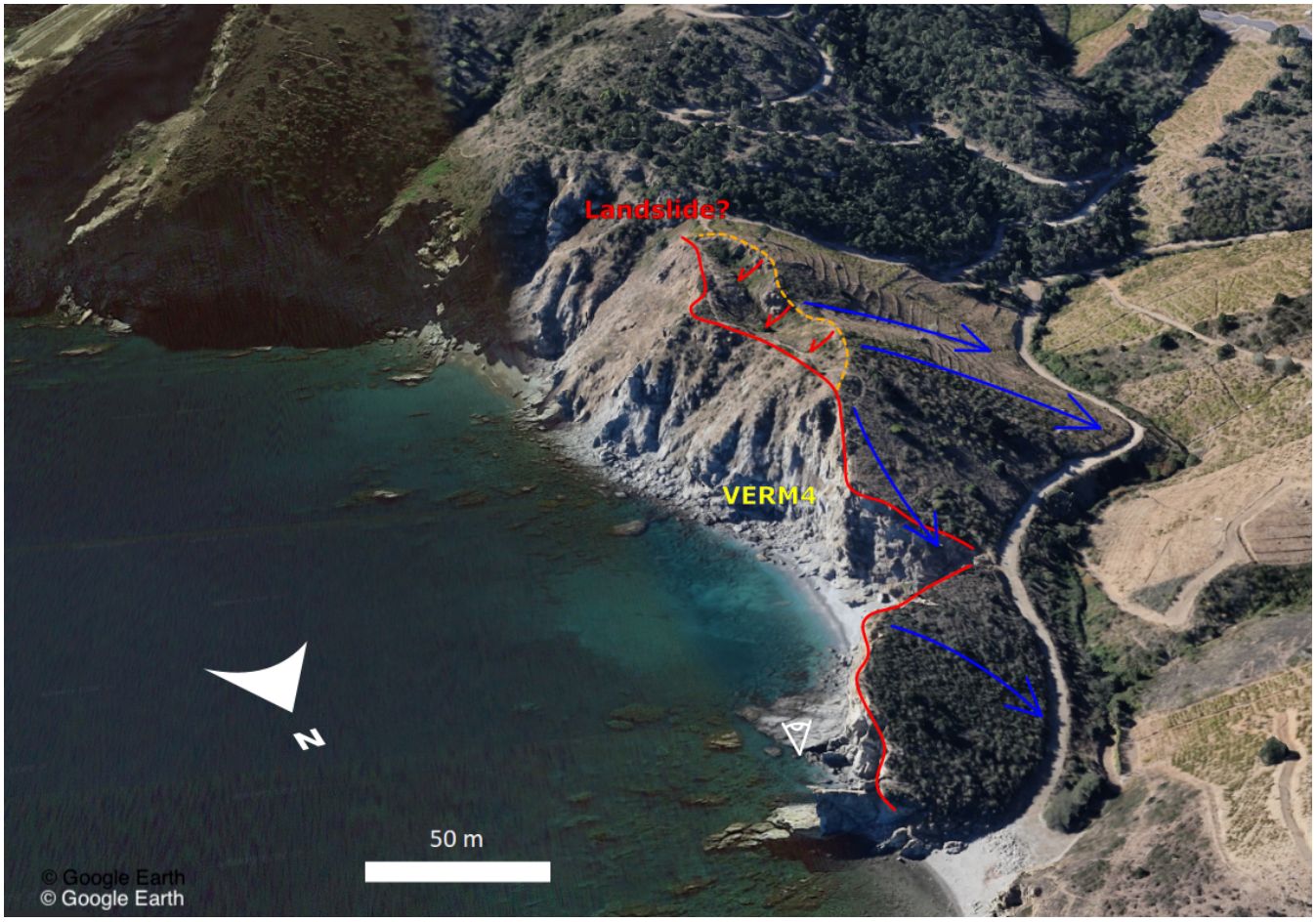

Figure S10. Interpreted 3D view (© Google Earth) of the cliff on the VERM4 sample site (yellow). Red lines are interpreted cliffs top. Orange dashed line is an interpreted crest line. Blue arrows are flow directions of the runoff water, interpreted from topography. Red arrows show the possible movement of the cliff. The white eye figure shows the location and the direction of the picture in Figure S9.

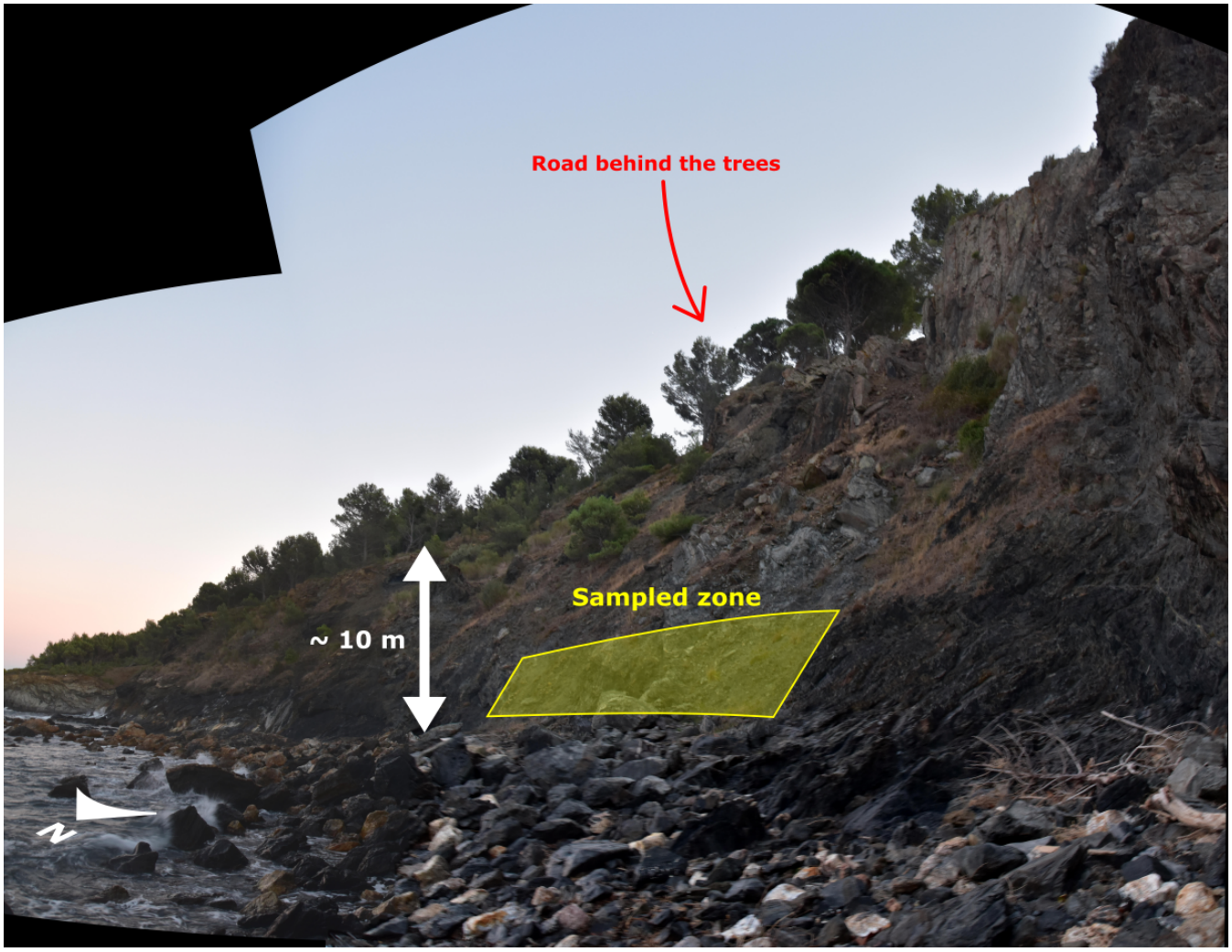

Figure S11. Mosaic picture of the VERM5 sample site, seen from north.

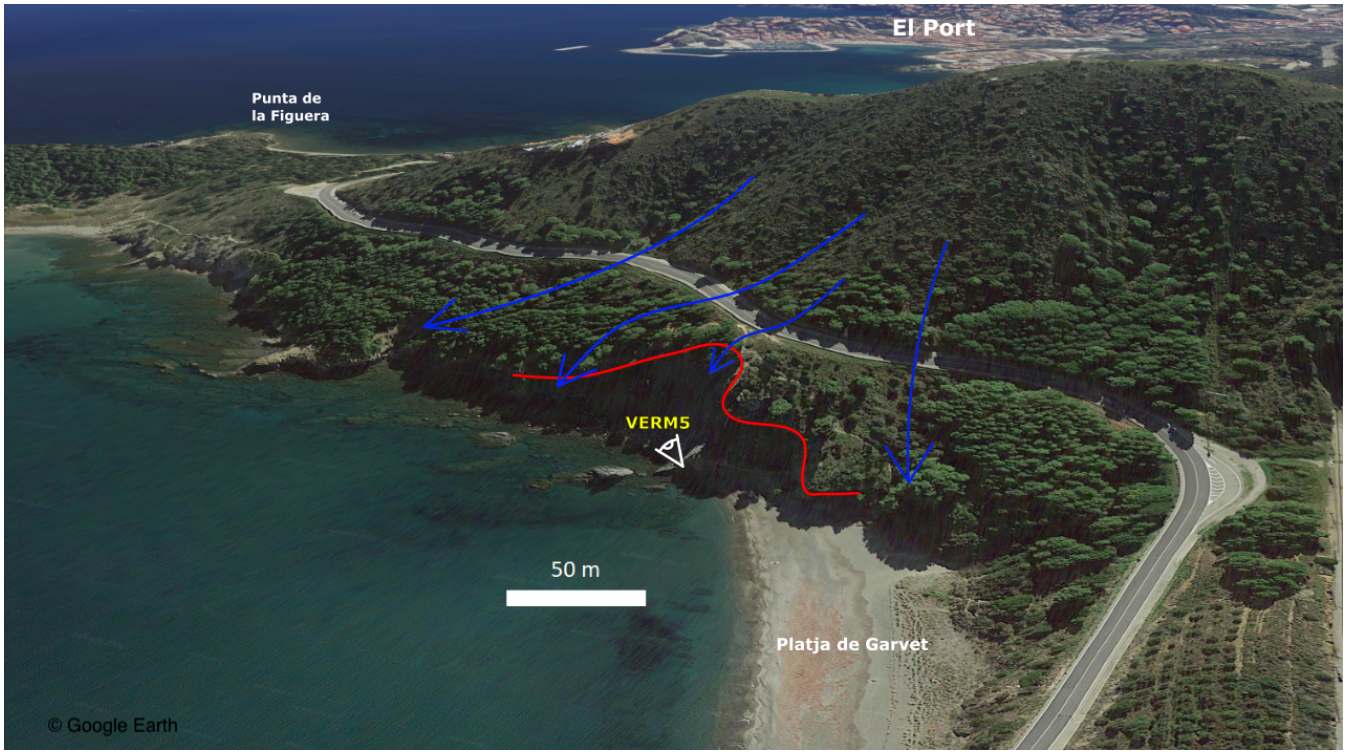

Figure S12. Interpreted 3D view (© Google Earth) of the cliff on the VERM5 sample site (yellow). The red line is the interpreted cliff top. Blue arrows are flow directions of the runoff water, interpreted from topography. The white eye figure shows the location and the direction of the picture in the Figure S11.

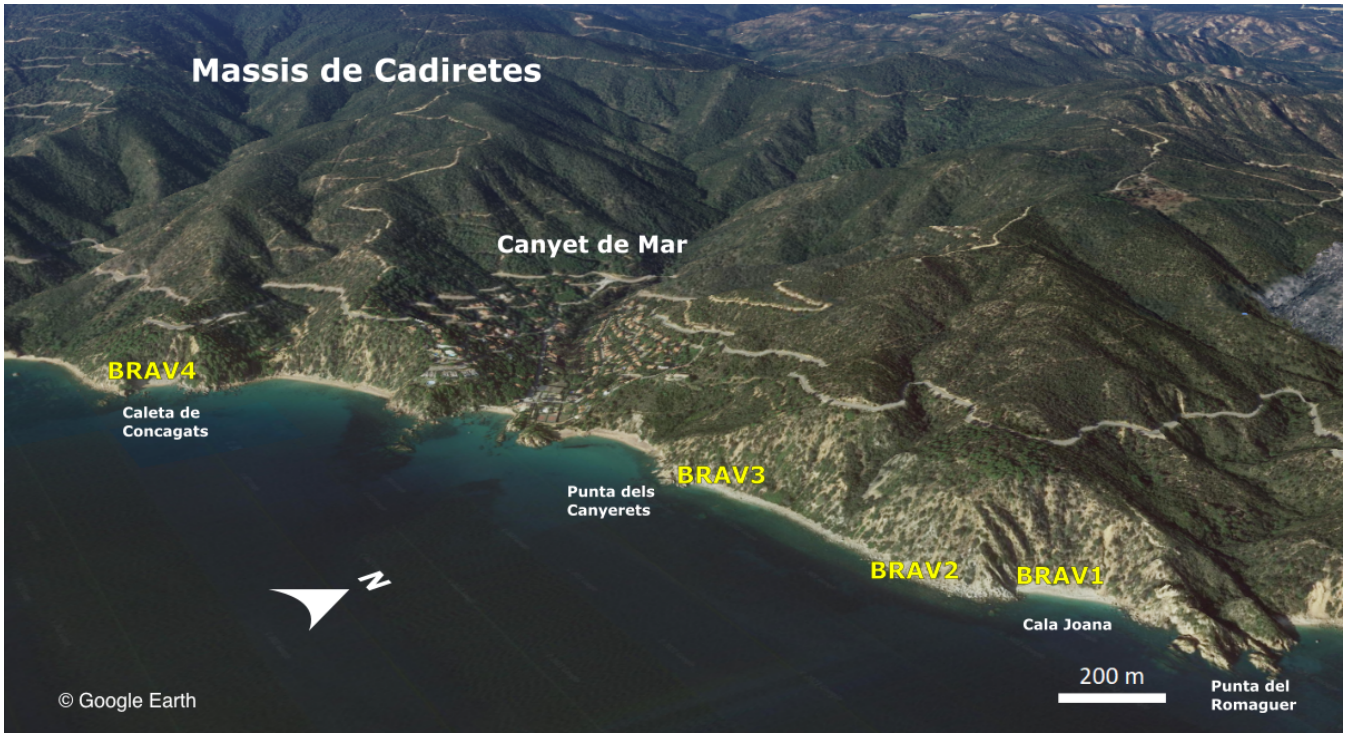

Figure S13. 3D view (© Google Earth) of the coast around Canyet de Mar. Locations of BRAV1, BRAV2, BRAV3 and BRAV4 are indicated in yellow.

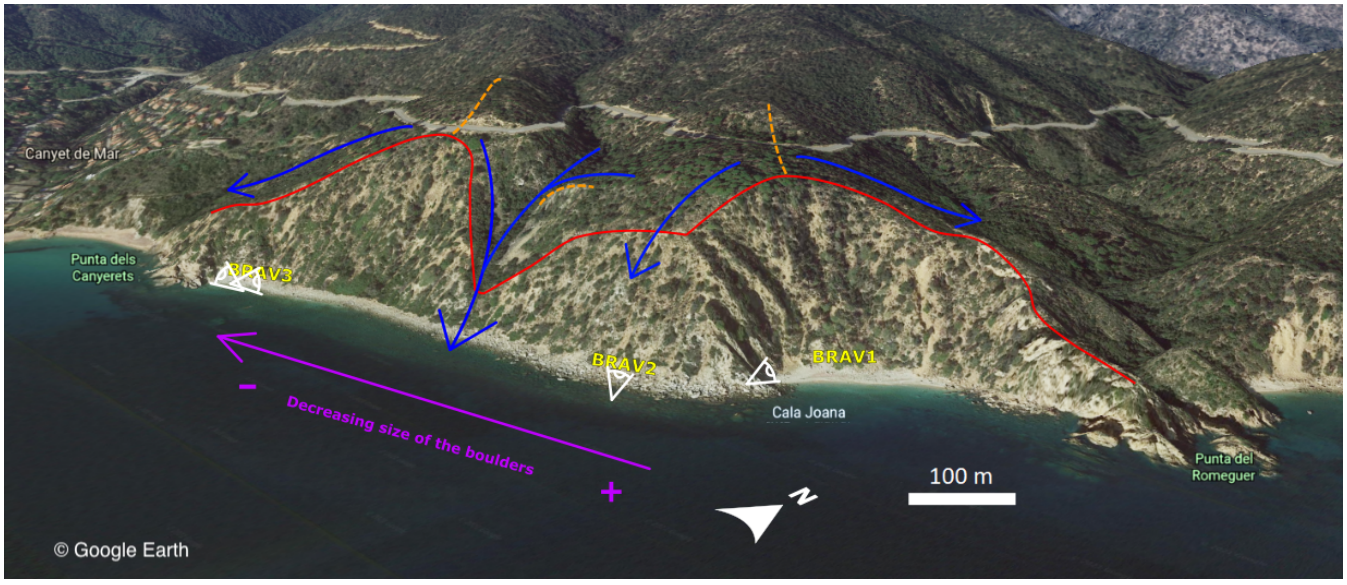

Figure S14. Interpreted 3D view (© Google Earth) of the cliffs for BRAV1, BRAV2 and BRAV3 (yellow). The red line is the interpreted cliff top. Orange dashed lines are interpreted crests lines. Blue arrows are flow directions of the runoff water, interpreted from topography. White eye figures show the location and the direction of the picture for each sample site. The purple arrow indicate the direction of the decreasing size of the boulders at the cliff base between BRAV2 and BRAV3 sample sites.

Figure S15. Mosaic picture of the BRAV1 sample site, seen from the southwest.

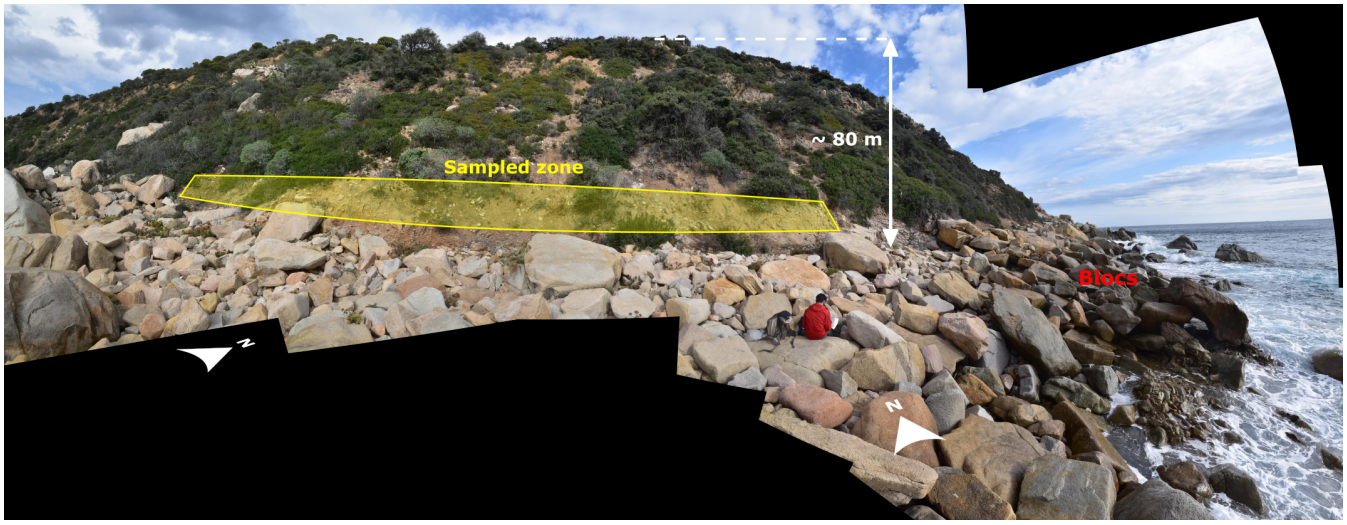

Figure S16. Mosaic picture of the BRAV2 sample site, seen from the south (facing the cliff).

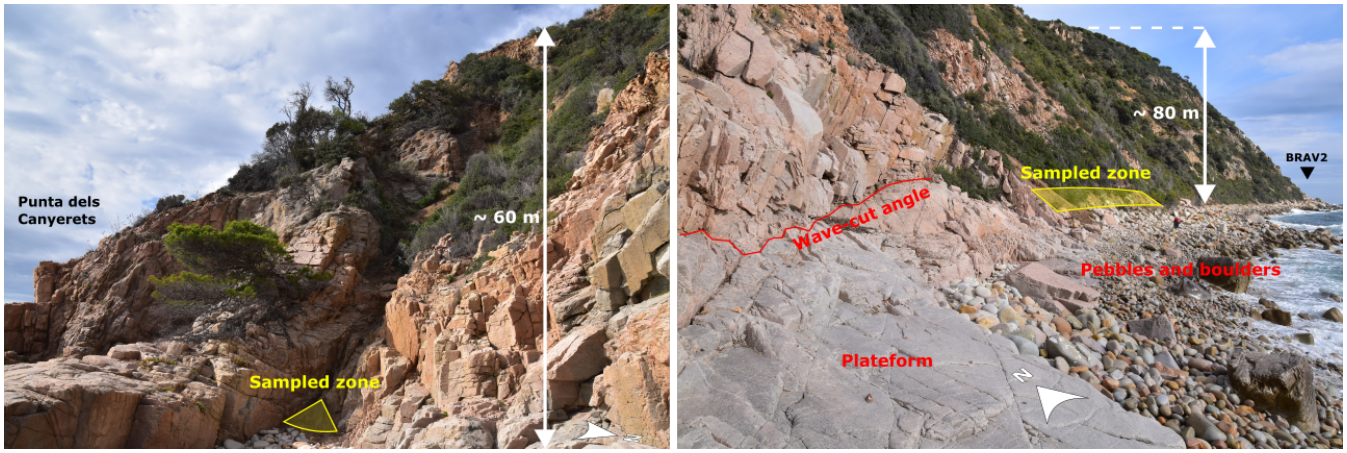

Figure S17. Interpreted pictures of the BRAV3 sample site, seen from the east (left) and the southwest (right).

Figure S18. Mosaic picture of the BRAV4 sample site, seen from the southwest.

Figure S19. Interpreted 3D view (© Google Earth) of the cliff for the BRAV4 sample site (yellow). The red line is the interpreted cliff top. The orange dashed line is an interpreted crest line. Blue arrows are flow directions of the runoff water, interpreted from topography. The white eye figure shows the location and the direction of the picture in the Figure S18.

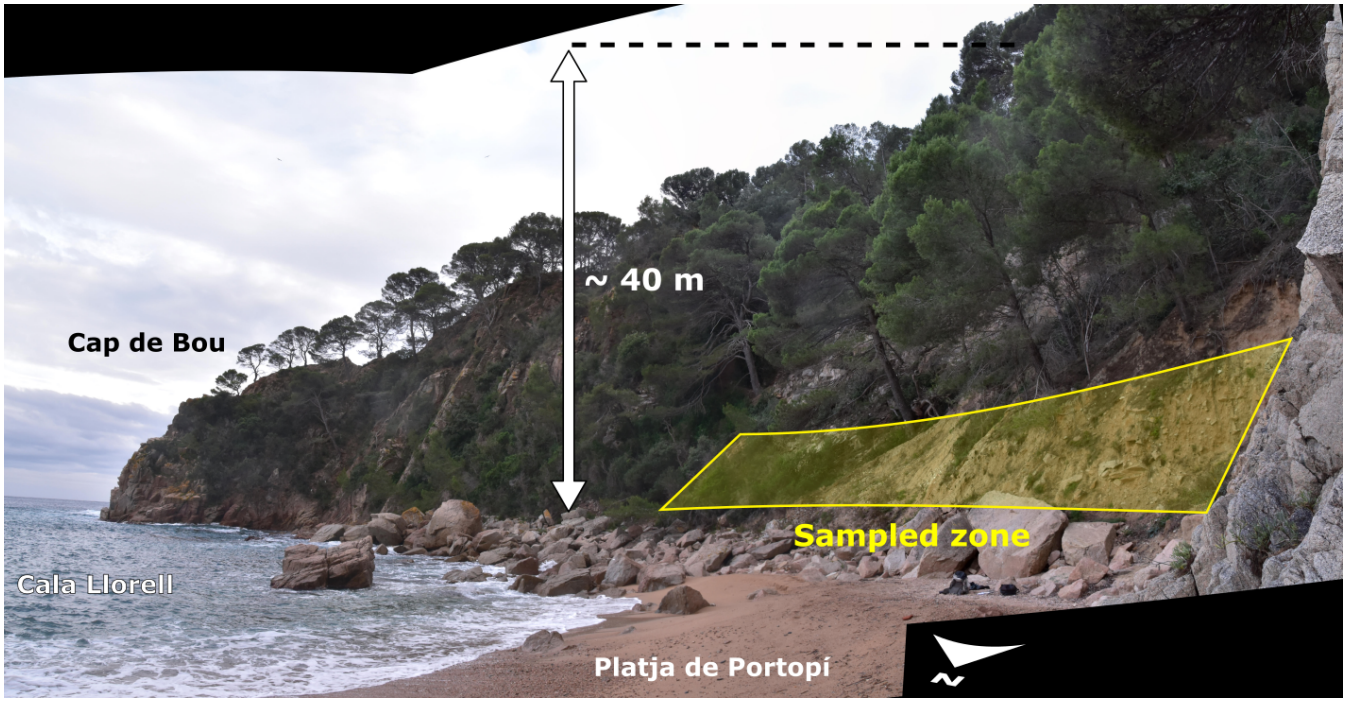

Figure S20. Mosaic picture of the BRAV5 sample site, seen from the north.

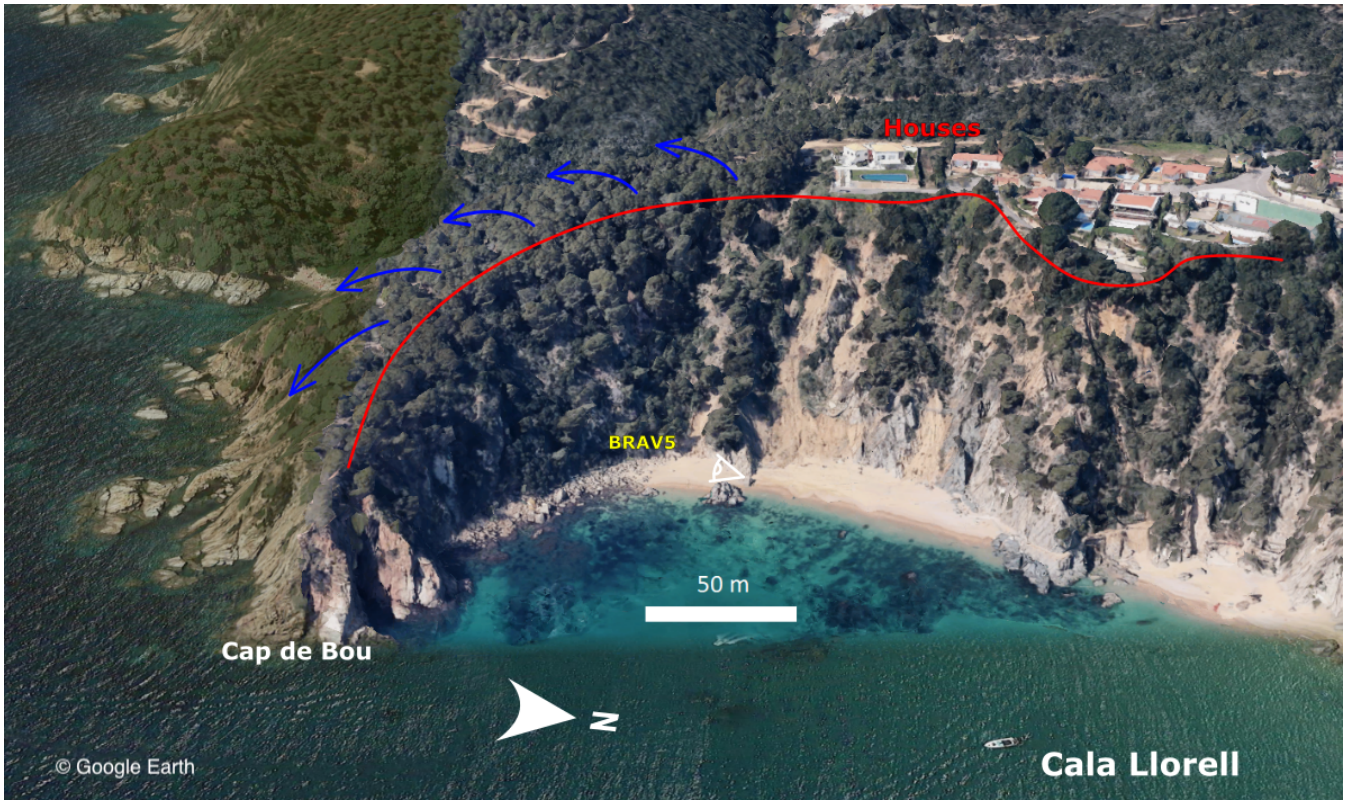

Figure S21. Interpreted 3D view (© Google Earth) of the cliff for the BRAV5 sample site (yellow). The red line is the interpreted cliff top. Blue arrows are flow directions of the runoff water, interpreted from topography. The white eye figure show the location and the direction of the picture in the Figure S20.

Figure S22. 3D view (© Google Earth) of the coast around Atico. Locations of COSTA1, COSTA2 and COSTA3 are indicated in yellow.

Figure S23. Picture of the COSTA1 sample site, seen from the east. The sampling has been performed well above any effect of the road cut.

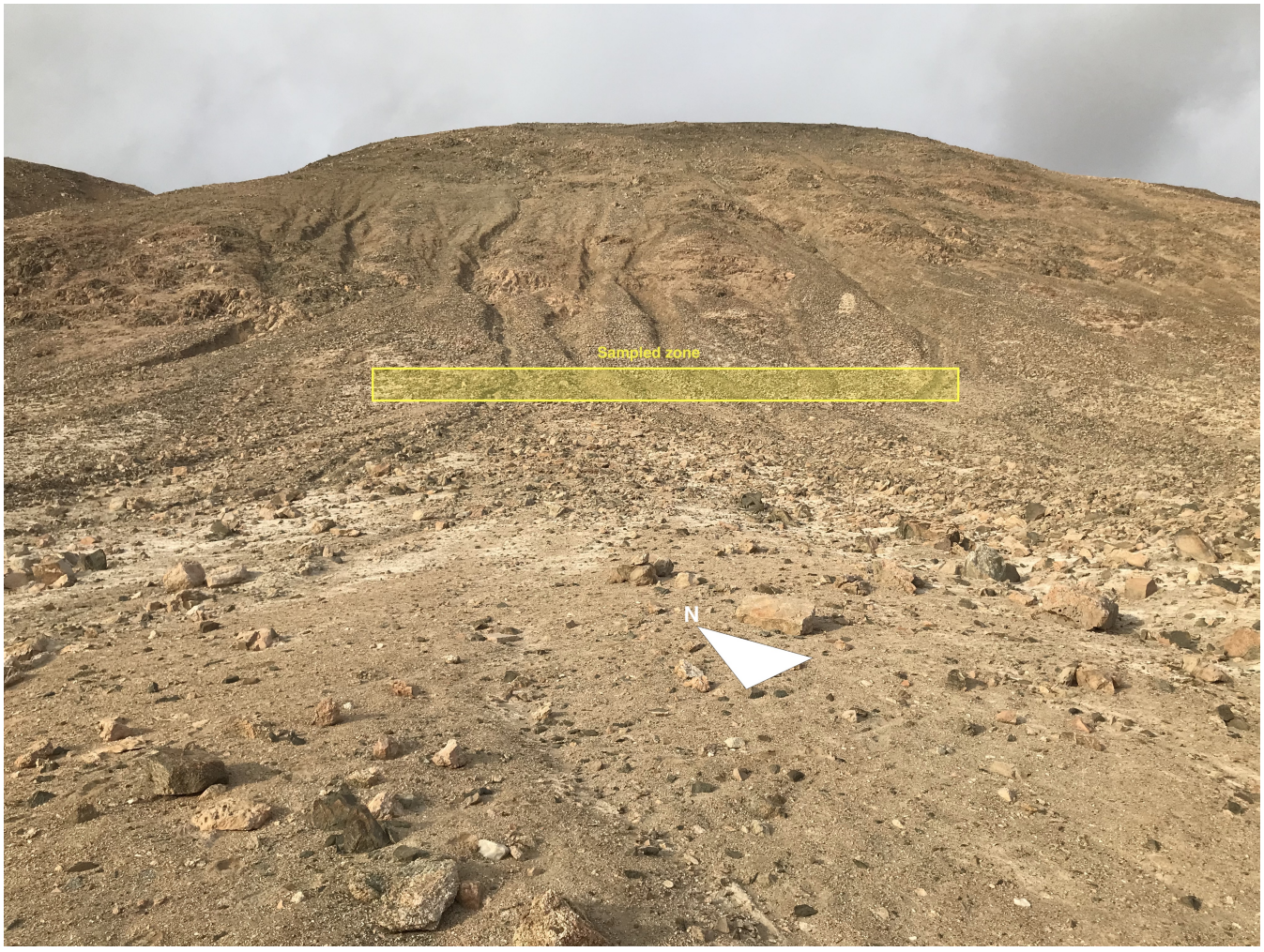

Figure S24. Picture of the COSTA3 sample site, seen from the south.

References

Arnold, M., Merchel, S., Bourlès, D. L., Braucher, R., Benedetti, L., Finkel, R. C., Aumaître, G., Gottdang, A., and Klein, M.: The French accelerator mass spectrometry facility ASTER: Improved performance and developments, Nuclear Instruments and Methods in Physics Research Section B: Beam Interactions with Materials and Atoms, 268, 1954–1959, https://doi.org/10.1016/j.nimb.2010.02.107, 2010.

Bintanja, R. and van de Wal, R. S. W.: North American ice-sheet dynamics and the onset of 100,000-year glacial cycles, Nature, 454, 869–872, https://doi.org/10.1038/nature07158, 2008.

Braucher, R., Brown, E. T., Bourles, D. L., and Colin, F.: In situ produced Be-10 measurements at great depths: implications for production rates by fast muons, Earth And Planetary Science Letters, 211, 251–258, 2003.

Braucher, R., Guillou, V., Bourlès, D. L., Arnold, M., Aumaître, G., Keddadouche, K., and Nottoli, E.: Preparation of ASTER in-house 10Be/9Be standard solutions, Nuclear Instruments and Methods in Physics Research Section B: Beam Interactions with Materials and Atoms, 361, 335–340, https://doi.org/10.1016/j.nimb.2015.06.012, 2015.

Chmeleff, J., von Blanckenburg, F., Kossert, K., and Jakob, D.: Determination of the Be-10 half-life by multicollector ICP-MS and liquid scintillation counting, Nuclear Instruments & Methods In Physics Research Section B-Beam Interactions With Materials And Atoms, 268, 192–199, 2010.

de Lange, W. P. and Moon, V. G.: Estimating long-term cliff recession rates from shore platform widths, Engineering Geology, 80, 292, 2005.

DiBiase, R. A.: Increasing vertical attenuation length of cosmogenic nuclide production on steep slopes negates topographic shielding corrections for catchment erosion rates., Earth Surface Dynamics, 6, 2018.

Korschinek, G., Bergmaier, A., Faestermann, T., Gerstmann, U., Knie, K., Rugel, G., Wallner, A., Dillmann, I., Dollinger, G., and von Gostomski, C. L.: A new value for the half-life of 10Be by Heavy-Ion Elastic Recoil Detection and liquid scintillation counting, Nuclear Instruments and Methods in Physics Research Section B: Beam Interactions with Materials and Atoms, 268, 187–191, https://doi.org/10.1016/j.nimb.2009.09.020, 2010.

Regard, V., Dewez, T., Bourlès, D. L., Anderson, R. S., Duperret, A., Costa, S., Leanni, L., Lasseur, E., Pedoja, K., and Maillet, G. M.: Late Holocene seacliff retreat recorded by 10Be profiles across a coastal platform: Theory and example from the English Channel, Quaternary Geochronology, 11, 87–97, https://doi.org/10.1016/j.quageo.2012.02.027, 2012.

Stephenson, W. J. and Kirk, R. M.: Development of shore platforms on Kaikoura Peninsula, South Island, New Zealand - Part one: The role of waves, Geomorphology, 32, 21–41, 2000.

Stone, J.: Air pressure and cosmogenic isotope production, J. Geophys. Res., 105, 23 753–23 759, https://doi.org/ISI:000089895700027, 2000.

Trenhaile, A. S.: Rock coasts, with particular emphasis on shore platforms, Geomorphology, 48, 7, 2002.